Springer

Journal of
Mechanical
Science and
Technology

Journal of Mechanical Science and Technology 23 (2009) 802~813

www.springerlink.com/content/1738-494x
DOI 10.1007/s12206-009-0115-z

Computational study on aerodynamics of long-span bridges †

Ilyong Yoo[1], Einkeun Kwak[1], Seungsoo Lee[1,*], Beom Soo Kim[1] and Si Hyong Park[2]

[1]*Department of Aerospace Engineering, Inha University, Incheon, 402-751, Korea*
[2]*MiasIT, Sungnam, 462-807, Korea*

(Manuscript Received June 18, 2008; Revised November 24, 2008; Accepted January 21, 2009)

Abstract

A numerical procedure for aerodynamic load analysis of long span bridges is presented. The preconditioned Reynolds averaged Navier-Stokes equations are adopted to compute flows over the bridges. To capture the turbulent characteristics of the flows, two equation turbulence models, Coakley's $q-\omega$ model and Menter's $k-\omega$ SST model, are used to compute the turbulent viscosity. A dual time stepping method in conjunction with the AF-ADI method is used to advance the solution in time. A loosely coupled method of the preconditioned RANS equations with the turbulence model equations is employed for fast computation without losing numerical stability. The numerical method for the aerodynamic load analysis is verified against well-known benchmark problems. Aerodynamic loads of two real bridges are computed with the method to demonstrate the usefulness of the method.

Keywords: Unsteady aerodynamics; Long-span bridge; Computational fluid dynamics; Preconditioning method; Reynolds averaged; Navier-stokes equations

1. Introduction

The prediction of aerodynamic load on bridges becomes crucial as the structural design of the bridges becomes precise. Experimental approaches using wind tunnels have been the choice of engineers due to difficulties in predicting the aerodynamic load. With recent advances in computational fluid dynamics (CFD), the engineers are now equipped with a new powerful tool to predict the aerodynamic load on the bridges in addition to the wind tunnel testing. With CFD tools, the turnaround time for the design cycle is getting shorter and the cost of the design is getting lower.

Aerodynamic analysis of long-span bridges is usually done with two-dimensional analysis because three-dimensional effects are limited to both ends of the bridges. Shirai and Ueda [1] employed a two-dimensional Reynolds averaged Navier-Stokes (RANS) method for self-oscillating bridge deck sections. A modified non-linear eddy viscosity model based on the $k-\varepsilon$ model was used for turbulent flow computations. Two bridge sections were investigated for the aeroelastic behavior. Larsen and Walther [2] studied the wind loading and the aeroelastic responses of five generic bridge deck sections in cross wind using a discrete vortex method for two-dimensional incompressible viscous flows.

In this paper, a preconditioned RANS method with two-equation turbulence models is used to compute unsteady turbulent flows over long span bridges. Coakley's $q-\omega$ model [3] and Menter's SST (shear stress transport) $k-\omega$ model [4] are used for turbulent flow simulations. It is well known that the convergence characteristics of the Navier-Stokes equations suffer from slowdown when the Mach number is low. This comes from the fact that the disparity in eigenvalues of the convective fluxes becomes large, as the Mach number is getting low. Preconditioning methods modify locally the eigenvalues so that the

† This paper was recommended for publication in revised form by Associate Editor Kyung-Soo Yang

*Corresponding author. Tel.: +82 32 860 7358, Fax.: +82 32 865 5401
E-mail address: slee@inha.ac.kr

convergence characteristics at low Mach number are enhanced compared to the unmodified Navier-Stokes equations. The preconditioning method proposed by Weiss and Smith [5] is adopted in this paper. A finite volume method is used to discretize the spatial derivatives of the preconditioned RANS equations and the two-equation turbulence model equations. Roe's approximate Riemann solver [6] in conjunction with MUSCL extrapolation [7] is used for the second order spatial discretization error. The preconditioning method, however, destroys the true unsteadiness due to the modified time term. Moreover, the linearization of non-linear fluxes introduces temporal errors when the AF-ADI (approximate factorization-alternate direction implicit) method [8] is applied. For time accurate computations, the dual time stepping method [9] is used to obtain time accurate solution. In the dual time stepping method, a fictitious time term added to the Navier-Stokes equations is used to march the solutions, so that the factorization error as well as the linearization error can be minimized. Also, it reduces the time lag error associated with the explicit boundary condition method that is used in this paper.

In this paper, we will first present the governing equations; the preconditioned RANS equations and the turbulence model equations. We will discuss the numerical methods used in this paper. Starting with the preconditioning method, the spatial discretization method and the temporal discretization method will be discussed. The explicit boundary condition method suitable for the preconditioned RANS equations will be presented later. A couple of computational examples will be used to verify our numerical method. Finally, computational examples for real bridges will be presented to show the versatility of our method.

2. Governing equations

2.1 Reynolds averaged navier-stokes equations

The compressible RANS equations with a two-equation turbulence model can be written in Cartesian coordinates as

$$\frac{\partial W}{\partial t} + \nabla \cdot \vec{F}_c = \nabla \cdot \vec{F}_d + S \,. \tag{1}$$

Here, W denotes the conservative flow variable vector

$$W = \left[\rho,\ \rho u_i,\ E,\ \rho s_k\right]^T , \tag{2}$$

where ρ, u_i and E are the density, the velocity components of the velocity vector, and the specific total energy, respectively. The superscript, T denotes the transpose of a vector. The turbulent variables can be either the turbulent velocity scale, $s_1 = q$ and the specific dissipation rate, $s_2 = \omega$ for Coakley's $q-\omega$ model or the turbulent kinetic energy, $s_1 = k$ and the specific dissipation rate, $s_2 = \omega$ for Menter's $k-\omega$ SST model. Also, $\vec{F}_c$ is the convective flux vector and $\vec{F}_d$ is the viscous flux vector. Their components are defined by

$$F_c = \left[\rho u_i,\ \rho u_i u_j + p\delta_{ij},\ \rho u_i (E+p),\ \rho u_i s_k\right]^T , \tag{3}$$

$$F_d = \left[0,\ \tau_{ij},\ \Omega_j,\ \left(\mu + \sigma_{s_k}\mu_t\right)\frac{\partial s_k}{\partial x_i}\right]^T , \tag{4}$$

where p is the static pressure and δ_{ij} is the Kronecker delta. σ_{s_1} and σ_{s_2} are the turbulent model constants whose values can be found in Ref [3] for Coakley's $q-\omega$ model and Ref [4] for Menter's $k-\omega$ SST model. The total stress tensor, τ_{ij} and the total energy flux vector, Ω_i are defined by

$$\tau_{ij} = \left(\mu + \mu_t\right)\left(\frac{\partial u_i}{\partial x_j} + \frac{\partial u_j}{\partial x_i}\right) - \frac{3}{2}\left(\mu + \mu_t\right)\frac{\partial u_k}{\partial x_k}\delta_{ij} , \tag{5}$$

$$\Omega_i = u_j \tau_{ji} + C_p\left(\frac{\mu_m}{\mathrm{Pr}} + \frac{\mu_t}{\mathrm{Pr}_t}\right)\frac{\partial T}{\partial x_i} , \tag{6}$$

where μ and μ_t are the molecular viscosity and the turbulent viscosity, respectively. k and k_t are the thermal molecular conductivity and the turbulent conductivity. They can be expressed by using the Prandtl numbers as $\mathrm{Pr} = C_p\mu / k$ and $\mathrm{Pr}_t = C_p\mu_t / k_t$. For air, $\mathrm{Pr} = 0.72$ and $\mathrm{Pr}_t = 0.9$ are used throughout this paper. The temperature, T and the pressure are related to the specific total energy by the equation of state for a perfect gas,

$$E = e + \frac{1}{2}u_i u_i \,, \quad p = \left(\gamma - 1\right)\rho e \,, \quad e = C_v T \,, \tag{7}$$

where e is the specific internal energy; C_p and C_v are the specific heats at constant pressure and volume, respectively. Here, $\gamma = C_p / C_v$ is the ratio of specific heats. For air, $\gamma = 1.4$ is used. The source term, which arises from the turbulence equations, can be defined by

$$S = [0,\ 0,\ S_1,\ S_2]^T, \tag{8}$$

where the exact form of S_1 and S_2 can be found in Ref. [3] and Ref. [4].

2.2 Two-equation turbulence models

Coakley's $q-\omega$ turbulence model uses the transport equations for the turbulent velocity scale, q, and the specific dissipation rate, ω, to estimate the eddy viscosity. The turbulent velocity scale and the specific dissipation rate are related to the more popular turbulent variables, the turbulent kinetic energy k and the turbulent dissipation rate, ε,

$$s_1 = q = \sqrt{k}\ ,\quad s_2 = \omega = \frac{\varepsilon}{k}, \tag{9}$$

The turbulent viscosity can be computed by using the Prandtl-Kolmogorov relation

$$\mu_t = C_\mu D_q \frac{\rho q^2}{\omega}, \tag{10}$$

where $C_\mu = 0.09$. When the $q-\omega$ model equation is integrated to the wall, the damping function is given by

$$D_q = 1 - \exp(-0.022 R_q)\ ,\quad R_q = \frac{\rho q y}{\mu}, \tag{11}$$

where y is the normal distance from the nearest wall. If the wall function boundary condition is used along the solid wall, the damping term is set to 1. One of the advantages in using the $q-\omega$ model over other two-equation models is its numerical robustness. Unlike the $k-\varepsilon$ model, the source terms are bounded near the solid wall. Also, it is known that the $q-\omega$ model is insensitive to the free-stream turbulent quantities.

The SST $k-\omega$ model of Menter is a hybrid model that combines Wilcox's $k-\omega$ model in the inner boundary layer and the $k-\varepsilon$ model in the outer region of the boundary layer using a blending function,

$$F_1 = \tanh\left[\min\left(\max\left(\frac{\sqrt{k}}{0.09\omega y};\frac{500\nu}{y^2\omega}\right);\frac{4\rho\sigma_{\omega 2}k}{CD_{k\omega}y^2}\right)\right]^4, \tag{12}$$

where the cross-diffusion terms is given by

$$CD_{k\omega} = \max\left[2\rho\sigma_{\omega 2}\frac{1}{\omega}\frac{\partial k}{\partial x_j}\frac{\partial \omega}{\partial x_j}, 10^{-20}\right]. \tag{13}$$

A limitation of the shear stress is introduced in adverse pressure gradient regions as realized in Eq. (14),

$$\nu_t = \frac{\mu_t}{\rho} = \frac{0.31k}{\max[0.31\omega;\Omega F_2]}, \tag{14}$$

where Ω is the magnitude of the vorticity vector and F_2 is defined by

$$F_2 = \tanh\left[\max\left(2\frac{\sqrt{k}}{0.09\omega y};\frac{500\nu}{y^2\omega}\right)\right]^2. \tag{15}$$

3. Governing equations

3.1 Preconditioning method

The time marching schemes based on the density-based method suffer convergence degradation due to the wide disparity in the particle velocity and the acoustic wave speeds at low Mach numbers. The preconditioning methods alter the acoustic wave speeds comparable to the magnitude of the particle velocity by changing the time derivative terms of the Navier-Stokes equations. Therefore, good convergence characteristics can be attained even at low Mach numbers. In this paper, the preconditioning method of Weiss and Smith is adopted to ensure good convergence characteristics at all speeds. The preconditioning method modifies the Navier-Stokes equations and the two-equation turbulence model equations as

$$\Gamma\frac{\partial Q}{\partial t} + \nabla\cdot\vec{F}_c = \nabla\cdot\vec{F}_d + S, \tag{16}$$

where Q is the primitive variable vector,

$$Q = \left[p_g,\ u, v,\ T,\ s_1, s_2\right]^T. \tag{17}$$

Here, the gauge pressure $p_g = p - p_{atm}$ is used instead of the static pressure. According to the study of Venkateswaran and Merkle [10], using the gauge pressure reduces the round-off error associated with low Mach number flows. The preconditioning matrix of Weiss and Smith for two-dimensional problems is given by

$$\Gamma = \begin{bmatrix} \Theta & 0 & 0 & -\frac{\rho}{T} & 0 & 0 \\ \Theta u & \rho & 0 & -\frac{\rho u}{T} & 0 & 0 \\ \Theta v & 0 & \rho & -\frac{\rho v}{T} & 0 & 0 \\ \Theta H - 1 & \rho u & \rho v & -\frac{\rho u_i u_i}{2T} & 0 & 0 \\ \Theta s_1 & 0 & 0 & -\frac{\rho s_1}{T} & \rho & 0 \\ \Theta s_2 & 0 & 0 & -\frac{\rho s_2}{T} & 0 & \rho \end{bmatrix}, \quad (18)$$

where the total enthalpy is defined by

$$H = \frac{E+p}{\rho}, \quad (19)$$

and the parameter, Θ which is related with the reference velocity, U_r is given by

$$\Theta = \frac{1}{U_r^2} + \frac{1}{C_p T}. \quad (20)$$

The reference velocity, U_r acts as a cut-off velocity above which the preconditioning method is turned off. The detailed definition of the reference velocity can be found in Ref. [10].

3.2 Spatial discretization

Upon applying the finite volume discretization, the semi-discretized governing equations are found to be

$$\Gamma \frac{\partial Q}{\partial t} = R, \quad (21)$$

where the residual is defined by

$$R = \frac{1}{V}\left\{ \left(\bar{F}\Delta S\right)_{i+1/2} - \left(\bar{F}\Delta S\right)_{i-1/2} + \left(\bar{F}\Delta S\right)_{j+1/2} - \left(\bar{F}\Delta S\right)_{j-1/2} \right\} + S. \quad (22)$$

In Eq. (22), the total flux vector is used to avoid messy mathematical expressions

$$\bar{F} = \bar{F}_c - \bar{F}_d = \vec{F}_c \cdot \hat{n} - \vec{F}_d \cdot \hat{n}, \quad (23)$$

where the generalized inviscid flux vector and the viscous flux vector are

$$\bar{F}_c = \begin{bmatrix} \rho v_n \\ \rho v_n u + p n_x \\ \rho v_n v + p n_y \\ (E+p) v_n \\ \rho v_n s_1 \\ \rho v_n s_2 \end{bmatrix}, \bar{F}_d = \begin{bmatrix} 0 \\ n_x \tau_{xx} + n_y \tau_{yx} \\ n_x \tau_{xy} + n_y \tau_{yy} \\ n_x \Omega_x + n_y \Omega_y \\ \left(\mu_m + \sigma_{s1}\mu_t\right)\hat{n} \cdot \nabla s_1 \\ \left(\mu_m + \sigma_{s2}\mu_t\right)\hat{n} \cdot \nabla s_2 \end{bmatrix}. \quad (24)$$

The normal velocity to the cell edge used in Eq. (24) is defined by

$$v_n = \hat{n} \cdot \vec{u} = n_x u + n_y v, \quad (25)$$

where $\hat{n}$ is the outward normal vector of the computational cell.

The Jacobian matrix of the preconditioned flux vector becomes $A_\Gamma = \Gamma^{-1} \partial \bar{F}_c / \partial Q$, and its eigenvalues are found to be

$$\lambda\left(A_\Gamma\right) = \left(v_n, v_n, v_n' + a', v_n' - a', v_n, v_n\right), \quad (26)$$

where

$$v_n' = \frac{v_n}{2}(\beta+1), \quad a' = \sqrt{\left\{\frac{v_n}{2}(\beta-1)\right\}^2 + U_r^2}, \quad \beta = \frac{U_r^2}{a^2}, \quad a = \sqrt{\frac{\gamma p}{\rho}}. \quad (27)$$

On the other hand, the eigenvalues of the original governing equations are

$$\lambda\left(\frac{\partial \bar{F}_c}{\partial Q}\right) = \left(v_n, v_n, v_n + a, v_n - a, v_n, v_n\right). \quad (28)$$

Note that the condition number of the preconditioned system becomes smaller compared to that of the original system. The condition number is defined by the ratio of the largest eigenvalue to the smallest eigenvalue in magnitude.

For numerically stable computations, the generalized inviscid flux vector is replaced with Roe's approximated Riemann solver as

$$\tilde{F}_{c_{i+1/2}} = \frac{1}{2}\left(\bar{F}_{c_i} + \bar{F}_{c_{i+1}} - \Gamma\left|A_\Gamma\right|\Delta Q\right). \quad (29)$$

The matrix product, $\Gamma\left|A_\Gamma\right|$ is evaluated with Roe's average. MUSCL (monotone upwind schemes for conservation laws) extrapolation together with the

minmod limiter or van Alabada's limiter is used for the second order of accuracy in order to maintain the TVD (total variation diminishing) property.

The spatial derivatives that are needed to evaluate viscous terms can be computed from the gradient theorem,

$$\nabla f = \frac{1}{V}\int_S f\hat{n}dS \,. \tag{30}$$

3.3 Temporal discretization

The semi-discretized equations, Eq. (21), show that the steady state solution does not depend upon the preconditioning matrix. However, Eq. (21) should be modified in order to solve unsteady problems. The dual time stepping method is applied to the preconditioned Navier-Stokes equations and the turbulence model equations,

$$\Gamma\frac{\partial Q}{\partial \tau} + \frac{\partial W}{\partial t} = R \,. \tag{31}$$

The preconditioning matrix is now pre-multiplied to the artificial time term instead of the time term as in Eq. (21). The discretized version of Eq. (31) is now given as

$$\begin{aligned}(1+\frac{\phi}{2})\frac{\Delta\overline{W}}{\Delta t} - \frac{\phi}{2}\frac{\Delta W^{n-1}}{\Delta t} + \Gamma\frac{\Delta Q^l}{\Delta\tau} \quad , \\ + \theta R^{l+1} + (1-\theta)R^n = 0\end{aligned} \tag{32}$$

where the corrections are defined by

$$\begin{aligned}\Delta\overline{W} &= W^{l+1} - W^l \,, \\ \Delta W^n &= W^{n+1} - W^n \,, \\ \Delta W^{n-1} &= W^n - W^{n-1} \,.\end{aligned} \tag{33}$$

The superscript n denotes the time step and the superscript l denotes the fictitious dual time step. The combinations of ϕ and θ give the different temporal accuracy of the scheme. In this paper, $\phi = 1$ and $\theta = 1$ are used, which gives second order accuracy in time.

Upon applying the alternating direction implicit (ADI) method, the resulting dual time stepping method can be written as

$$L_i D^{-1} L_j \Delta Q = -\Delta\tau\overline{R} \,, \tag{34}$$

where the operators are given by

$$\begin{aligned}L_i = D + \frac{\theta\Delta\tau}{V}\Bigg\{&\left(\frac{\partial\overline{F}_{i+1/2}}{\partial Q_{i+1}} + \frac{\partial\overline{F}_{i+1/2}}{\partial Q_i}\right)\Delta S_{i+1/2} \\ &- \left(\frac{\partial\overline{F}_{i-1/2}}{\partial Q_i} + \frac{\partial\overline{F}_{i-1/2}}{\partial Q_{i-1}}\right)\Delta S_{i-1/2}\Bigg\} \,,\end{aligned} \tag{35}$$

$$\begin{aligned}L_j = D + \frac{\theta\Delta\tau}{V}\Bigg\{&\left(\frac{\partial\overline{F}_{j+1/2}}{\partial Q_{j+1}} + \frac{\partial\overline{F}_{j+1/2}}{\partial Q_j}\right)\Delta S_{j+1/2} \\ &- \left(\frac{\partial\overline{F}_{j-1/2}}{\partial Q_j} + \frac{\partial\overline{F}_{j-1/2}}{\partial Q_{j-1}}\right)\Delta S_{j-1/2}\Bigg\} \,.\end{aligned} \tag{36}$$

Only destruction terms of the turbulence source terms are treated implicitly for stability reason as described in Ref. [11]. The matrices D, M and K are given by

$$\begin{aligned}D &= (1+\frac{\phi}{2})M\frac{\Delta\tau}{\Delta t} + \Gamma - \theta\Delta\tau K \,, \\ M &= \frac{\partial W}{\partial Q} \,, \quad K = \frac{\partial S}{\partial W} \,.\end{aligned} \tag{37}$$

The unsteady residual defined by

$$\begin{aligned}\overline{R} = (1+\frac{\phi}{2})\frac{W^l - W^n}{\Delta t} - \frac{\phi}{2}\frac{W^n - W^{n-1}}{\Delta t} \\ + \theta R^l + (1-\theta)R^n \,.\end{aligned} \tag{38}$$

After convergence, we have

$$W^{l+1} = W^l = W^{n+1} \,. \tag{39}$$

Therefore, $\overline{R} = 0$. These are the discretized equations of the unsteady governing equations. This implies that the solutions with the present method are independent of the preconditioning matrix and $\Delta\tau$. Equation (32) can be applied to steady problems with $C_1 = 1 + \phi/2 = 0$, $C_2 = \phi/2 = 0$, and $\tau = t$.

Eq. (32) is a set of discretized equations of RANS equations and the turbulence model equations. It can be solved either by a loosely coupled method or by a strongly coupled method. The loosely coupled method solves the Navier-Stokes equations and the turbulence model equations in sequence, while the strongly coupled method solves two sets of equations simultaneously. According to Lee and Choi [11], the stability characteristics of the loosely coupled method were the same as that of the strongly coupled method. Also, they showed that the actual convergence characteristics were the same through the number of computational examples. In this study, we adopt the

loosely coupled method since it runs faster and its implementation is relatively simple compared to the strongly coupled method.

3.4 Boundary conditions

Ghost cells are fictitious cells that are placed outside the physical boundaries in order to simplify application of the boundary conditions. A non-reflecting boundary condition method is employed to suppress unwanted wave reflections at the boundaries. The non-reflecting boundary condition method takes the direction of wave propagation into account when applying boundary conditions. The characteristic variables are prescribed or extrapolated depending on the sign of wave directions. Let variables with a subscript 'b' denote variables to be computed at the ghost cells. Variables with a subscript '∞' denote the freestream values, while variables with a subscript 'i' denote flow variables extrapolated from the interior domain. At the subsonic inlet boundary, five eigenvalues are positive, and one eigenvalue is negative, which suggests that five characteristic variables be prescribed and that one characteristic variable be extrapolated. That is,

$$p_b = \frac{1}{2}\left\{ p_\infty + p_i - sign(\lambda_1)\rho a'\left(v_{n_\infty} - v_{n_i}\right)\right\}, \tag{40}$$

$$T_b = T_\infty - \frac{p_\infty - p_b}{\rho C_p}, \tag{41}$$

$$u_b = u_\infty - \frac{(p_\infty - p_b)n_x}{\rho\left\{\frac{v_n}{2}(\beta-1) + sign(\lambda_1)a'\right\}}, \tag{42}$$

$$v_b = v_\infty - \frac{(p_\infty - p_b)n_y}{\rho\left\{\frac{v_n}{2}(\beta-1) + sign(\lambda_1)a'\right\}}, \tag{43}$$

$$q_b = q_\infty, \tag{44}$$

$$\omega_b = \omega_\infty, \tag{45}$$

where $sign(\lambda_1)$ is used to account for the definition of the normal vector, $\hat{n}$. At the subsonic outflow boundary, however, five characteristic variables are extrapolated, and one characteristic variable is prescribed:

$$p_b = \frac{1}{2}\left\{ p_\infty + p_i - sign(\lambda_1)\rho a'\left(v_{n_\infty} - v_{n_i}\right)\right\}, \tag{46}$$

$$T_b = T_i - \frac{p_i - p_b}{\rho C_p}, \tag{47}$$

$$u_b = u_i - \frac{(p_i - p_b)n_x}{\rho\left\{\frac{v_n}{2}(\beta-1) + sign(\lambda_1)a'\right\}}, \tag{48}$$

$$v_b = v_i - \frac{(p_i - p_b)n_y}{\rho\left\{\frac{v_n}{2}(\beta-1) + sign(\lambda_1)a'\right\}}, \tag{49}$$

$$q_b = q_i, \tag{50}$$

$$\omega_b = \omega_i. \tag{51}$$

If the turbulence model equations are integrated to the wall, we use the non-slip boundary conditions for the mean flow. For the $q-\omega$ model, the turbulent velocity scale is set to zero at the wall, while the normal gradient of the specific dissipation rate is set to zero at the wall,

$$\left.\frac{\partial q}{\partial n}\right|_w = 0, \quad \omega_w = 0. \tag{52}$$

For the $k-\omega$ model, the turbulent kinetic energy is set to zero and the normal gradient of the specific dissipation rate is given by

$$k_w = 0, \quad \left.\frac{\partial \omega}{\partial n}\right|_w = \frac{60\mu}{\beta_1 y^2}, \tag{53}$$

where y is the normal distance from the wall, and β_1 is the model constant of the $k-\omega$ model. For the $q-\omega$ model, the wall function method is available where the slip wall boundary condition is used for the mean flow. The amount of slip is determined to give the same value of wall shear stress computed from the wall function. The turbulent velocity scale and the specific dissipation rate are evaluated with the following equations:

$$q = \frac{u_\tau}{\sqrt[4]{C_\mu}}, \quad \omega = \frac{\sqrt{C_\mu}u_\tau}{k_v y}, \tag{54}$$

where u_τ is the friction velocity that is determined from the wall function and k_v is the von Karman constant of 0.41. The pressure and the temperature at the wall can be computed from the boundary layer approximation and the adiabatic temperature condition,

$$\left.\frac{\partial p}{\partial n}\right|_w = 0, \quad \left.\frac{\partial T}{\partial n}\right|_w = 0. \tag{55}$$

4. Computational results

4.1 Laminar flow around a circular cylinder

Laminar flow around a circular cylinder is chosen to show the accuracy of the present method for unsteady problems. Fig. 1 shows an O-type computational grid of 257×257. The Reynolds number based on the diameter of the cylinder is 150 and the Mach number is 0.2. It is well known that the flow over the circular cylinder becomes unsteady if $\mathrm{Re} > 40$ and that the so-called Karmann vortex street is formed behind the cylinder. The vortex shedding frequency is well correlated to the free stream velocity via Strouhal number, $St = fD/U_\infty$ where f is the shedding frequency of vortices, D is the diameter of the cylinder, and U_∞ is the free-stream velocity.

The initial condition for the unsteady computation is obtained after 1,000 steady iterations with an angle of attack of 10 degrees. Then, the unsteady computation is performed with an angle of attack 0 degree. This creates asymmetry in the solution so that the vortex shedding forms more easily. The number of the inner iterations for the dual time stepping method is 30, and the time step for the unsteady computation in terms of non-dimensionalized time is $\Delta t^* = \Delta t a_\infty / D = 0.005$. Fig. 2 presents the time histories of the aerodynamic coefficients over the cylinder. The Strouhal number computed from the time history of the lift coefficient is found to be $St = 0.1826$. Also, the quantitative comparisons of both C_d and C_l with Ref. [12] are presented in the Table 1. The drag coefficient and the lift coefficient are defined by

$$C_d = \frac{2\cdot F_x}{\rho\cdot U_\infty^2\cdot D},\quad C_l = \frac{2\cdot F_y}{\rho\cdot U_\infty^2\cdot D}. \tag{56}$$

Figs. 3 and 4 show the velocity magnitude contour lines and streaklines at the maximum lift coefficients. Unsteady vortex flow due to the flow separation from the surface of the cylinder and its shedding vortices are clearly shown through those figures. To check the solution convergence, the same computations are repeated with three different grids: 129×129, 257×257, and 350×350. Table 2 shows the computational results with the grids indicating the convergence of the solution.

Table 1. Comparison of the aerodynamic characteristics over the circular cylinder.

	St	C_d	C_l
Present Method	0.1826	1.327 ± 0.024	±0.515
Ref. 12	0.182	1.334 ± 0.03	±0.530

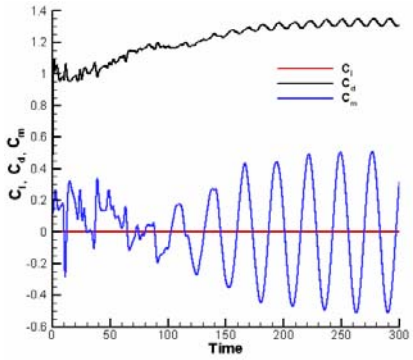

Fig. 2. Time histories of the aerodynamic coefficients of the circular cylinder, $M = 0.1$, $\mathrm{Re} = 150$.

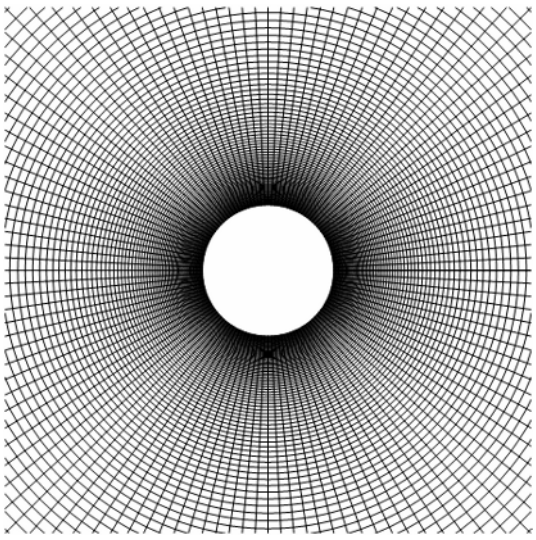

Fig. 1. Close-up view of an O-type grid over a cylinder.

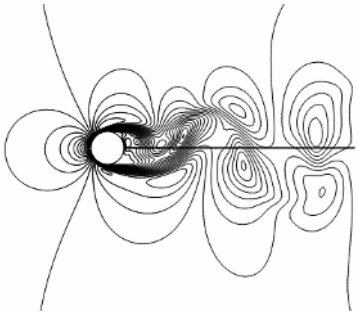

Fig. 3. Instant velocity magnitude contour lines at the maximum lift.

Table 2. Grid convergence of the aerodynamic characteristics over the circular cylinder.

	Grid size	St	C_d	C_l
Coarse	129×129	0.1810	1.322 ± 0.026	±0.515
Medium	257×257	0.1825	1.333 ± 0.034	±0.538
Fine	350×350	0.1825	1.333 ± 0.031	±0.540

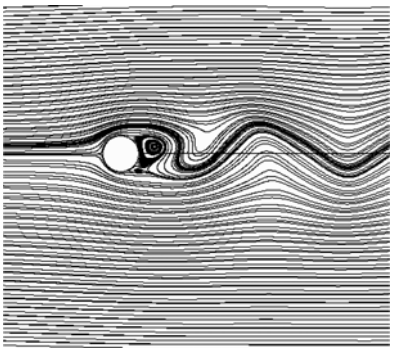

Fig. 4. Instant streaklines over the cylinder at the maximum lift.

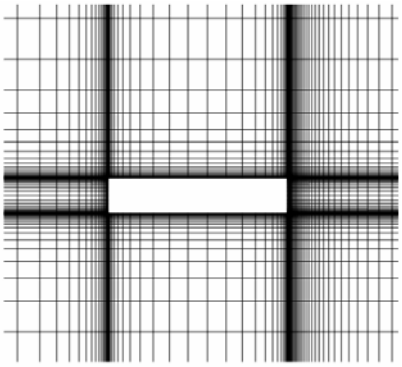

Fig. 5. Close-up view of grid system over a rectangular cylinder.

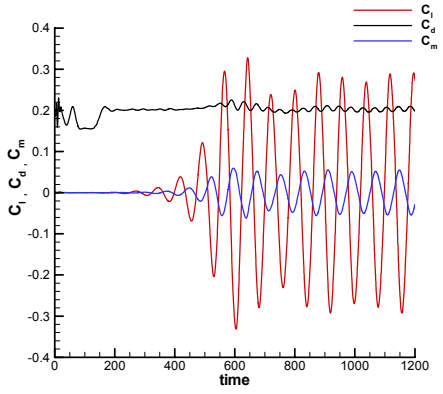

Fig. 6. Time histories of aerodynamic coefficients of the rectangular cylinder $M = 0.0294$, $\mathrm{Re} = 10^5$.

Table 3. Comparison of the aerodynamic characteristics over the rectangular cylinder.

	St	$C_{d,mean}$	$C_{l,\max}$
Present Method	0.087	0.20	0.28
Ref. 13	0.09	0.23	0.24

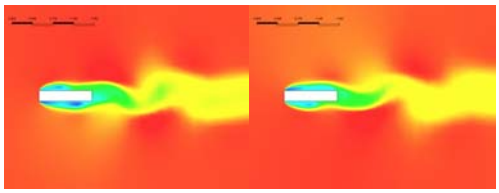

(a) $t^* = 600$ (b) $t^* = 650$

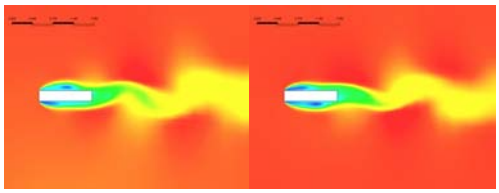

(c) $t^* = 700$ (d) $t^* = 750$

Fig. 7. Instant total pressure contour lines.

4.2 Turbulent flow over a rectangular cylinder

As the second verification problem, a turbulent flow over a rectangular cylinder is computed and compared with Larsen [13]. The aspect ratio of the cylinder is 5. The Mach number and the Reynolds number based on the length of the cylinder are 0.0294 and 10^5, respectively. Coakley's $q-\omega$ is chosen for the turbulent viscosity. The non-dimensional time increment is set to $\Delta t^* = 0.5$. The computational domain is divided into 10 blocks and the total number of grid points is 9,900. The turbulence model equations are integrated to the solid wall. In Figure 5, the grid system over the cylinder is shown. Unlike the previous case, the computation starts with a uniform flow. As can be seen in Fig. 6, it takes longer time to form shedding vortices that are emanating from the leading edges of the cylinder. In Table 3, Strouhal number, the mean drag coefficient and the mean lift coefficient are listed for comparison with Ref. [13]. Fig. 7 shows the total pressure contour plots in series at every 50 non-dimensional time. The flow-field patterns indicate separation bubbles near the leading edges. The formation of the separation bubbles alternates between the upper surface and the lower surface.

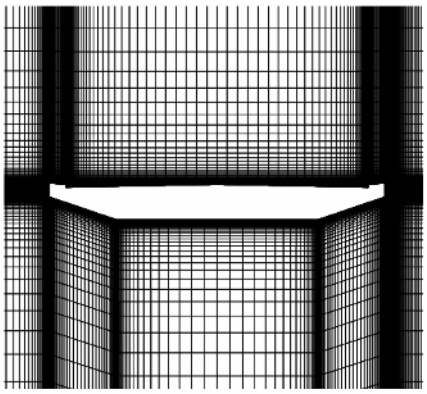

Fig. 8. Close-up view of grid system over the symmetric bridge deck section.

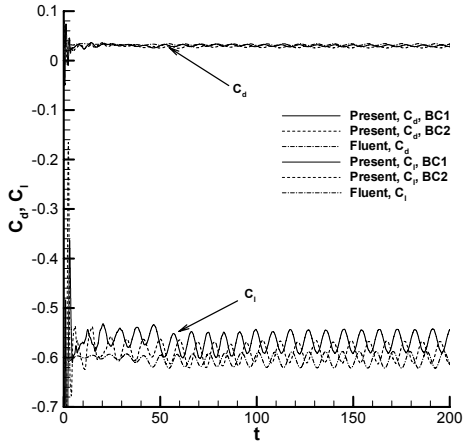

Fig. 9. Time histories of the aerodynamic coefficients of the symmetric bridge deck section M=0.0294, Re= 2×10^7 .

Also, the separation bubbles are convected downstream resulting in asymmetric flow pattern, which can be seen in Fig. 7.

4.3 Turbulent flow around a symmetric bridge deck section

As the first example of turbulent flow over a realistic bridge, a symmetric bridge deck section is selected. The grid system over the bridge deck section consists of 5 blocks and the blocks are 151×40, 389×70, 349×70, 101×20, and 61×40. Fig. 8 shows a close-up view of the grid system. The unsteady calculation starts with the initial condition that is computed with the initial steady run. The unsteady analysis is performed with non-dimensionalized time step, $\Delta t^* = 0.05$ and 10 inner time steps for the dual time stepping. Mach number and Reynolds number based on the length of the bridge deck section are 0.0294 and 2×10^7, respectively. Coakley's $q-\omega$ model is used with the wall function boundary condition. The wall function method is used to enforce the boundary condition along the surfaces of the bridge deck section.

Table 4. Time averaged aerodynamic coefficients of the symmetric bridge deck section.

	C_d	C_l
Present Method BC1	0.0298	-0.5665
Present Method BC2	0.0274	-0.5893
Fluent	0.0323	-0.6046

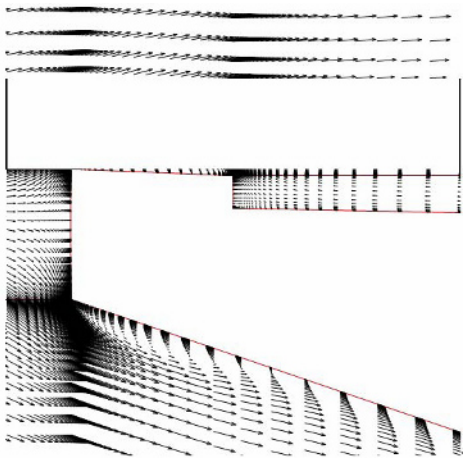

Fig. 10. Velocity vector plot near the leading edge of the bridge deck.

The time histories of aerodynamic coefficients are plotted in Fig. 9. Fluent [14], a widely used commercial solver for fluid dynamics, is used for comparison. The numerical methods used for Fluent are the PISO algorithm for pressure-velocity coupling, PRESTO for a pressure discretization and second-order upwind for momentum equations. Moreover, the RNG (renormalized group) $k-\varepsilon$ model with the wall function boundary is chosen for the turbulent viscosity. Since the available boundary conditions of Fluent are limited for subsonic flows, the symmetry conditions are stipulated on upper and lower boundaries in Fig. 8. However, this boundary condition is incorrect physically. The physically correct boundary condition should be that all the outer boundaries are far-field boundaries (BC1). For comparison purpose, the same boundary condition used in Fluent (BC2) is also used in computations. Figure 9 presents the histories of the

aerodynamic force and moment coefficients. Small differences in solutions between the present method and Fluent result from the fact that the present method uses a density-based method, while Fluent uses a pressure-based method. Nevertheless, Fig. 9 indicates that the results with BC2 match better with those of Fluent than those with BC1. However, the results with BC1 are believed to be physically correct. In Table 4, the averaged values of the aerodynamic coefficients are compared with each other. Figure 10 depicts the velocity vector field near the leading edge of the bridge. Large separation bubbles are formed not only at the upper deck of the bridge but also at the lower deck of the bridge.

4.4 Turbulent flow around an asymmetric bridge deck section

An asymmetric bridge deck section is chosen as the second example. The geometry of the second bridge deck section is more complex than that of the first bridge due to an extra pier that divides the upper deck of the bridge into two sections. The structured grid system depicted in Fig. 11 is divided into 22 blocks and the total number of grid points is 75,835. The Mach number used in the computation is 0.0294 and the Reynolds number based on the length of the bridge is 1×10^7. Menter's SST $k-\omega$ turbulence model is used for the turbulent viscosity. Numerical methods for Fluent are the same as in the previous computation.

Fig. 12 shows the periodic variations of the aerodynamic coefficients in time. Even though the magnitude of oscillation of the normal force coefficient shows a little difference, the averaged values of the present method and Fluent show good agreement as can be seen in Table 5. Both Figs. 13 and 14 show the velocity vector plots at two time instants. The two figures indicate that the large vortex formed at the end

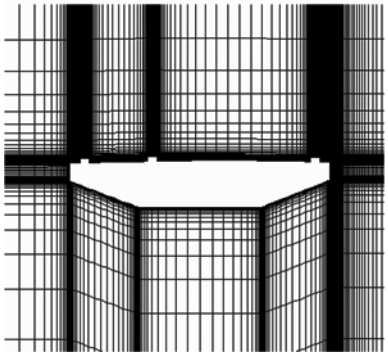

Fig. 11. Close-up view of grid system over the asymmetric bridge deck section.

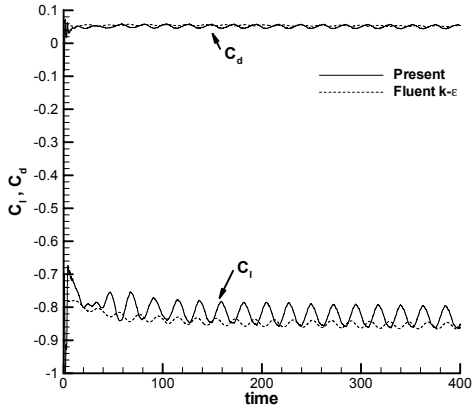

Fig. 12. Time histories of the aerodynamic coefficients of the asymmetric bridge deck section $M=0.0294$, $\mathrm{Re}=1\times10^7$.

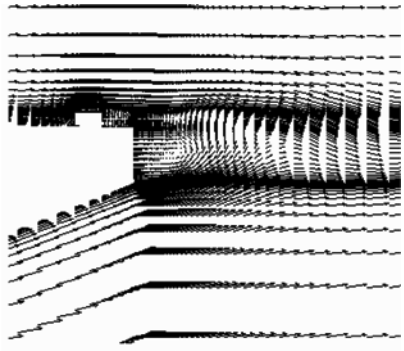

Fig. 13. Velocity vector plot near the trailing edge of the bridge deck showing large vortices induced from flow separation, $t^*=150$.

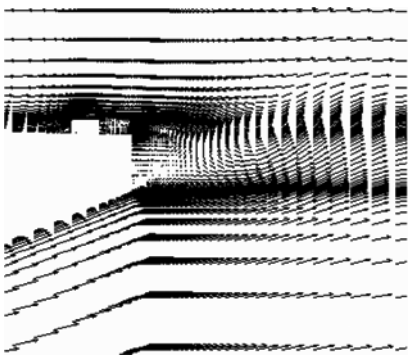

Fig. 14. Velocity vector plot near the trailing edge of the bridge deck showing large vortices moving downstream, $t^*=250$.

Table 5. Time averaged aerodynamic coefficients of the asymmetric bridge deck section.

	C_d	C_l
Present Method	0.0506	-0.825
Fluent $k-\varepsilon$	0.0535	-0.850

of deck moves downstream. It is found from the nu merical computation that several vortices are formed behind the piers and inside the cavities.

5. Conclusions

This paper presents a numerical method for computing aerodynamics of long-span bridges. The preconditioned RANS equations are used as governing equations. Two turbulence models are used to compute the turbulent eddy viscosity. Roe's approximated Riemann solver in conjunction with the finite volume method is adopted for spatial discretization. AF-ADI with the dual time stepping method is used to update the solution in a time accurate manner. Through validation problems and demonstration problems, it is found that the current numerical method is capable of accurately predicting the aerodynamics of a long span bridge deck.

Acknowledgment

This work was supported by Inha Univeristy research grant.

References

[1] S. Shirai and T. Ueda, Aerodynamic Simulation by CFD on Flat Box Girder of Super-Long-Span Suspension Bridge, *Journal of Wind Engineering and Industrial Aerodynamics*, 91 (1-2) (2003) 279-290.

[2] A. Larsen and J. H. Walther, Discrete Vortex Simulation of Flow around Five Generic Bridge Deck Sections, *Journal of Wind Engineering and Industrial Aerodynamics*, 77-78 (1998) 591-602.

[3] T. J. Coakley, Turbulence Modeling Methods for the Compressible Navier-Stokes Equations, AIAA paper 83-1693, 1983.

[4] F. R. Menter, Two-Equation Eddy-Viscosity Turbulence Models for Engineering Applications, *AIAA Journal*, 32 (8) (1994) 1598-1605.

[5] J. M. Weiss and W. A. Smith, Preconditioning Applied to Variable and Constant Density Flows, *AIAA Journal*, 33 (11) (1995) 2050-2057.

[6] R. L. Roe, Approximate Riemann Solvers, Parameter Vectors and Difference Schemes, Journal of Computational Physics, 43 (2) (1981) 357-372.

[7] B. Van Leer, Towards the Ultimate Conservative Difference Scheme. V. A Second Order Sequel to Godunov's Method, *Journal of Computational Physics*, 32 (1) (1976) 101-136.

[8] R. M. Beam and R. F. Warming, Implicit Numerical Methods for the Compressible Navier-Stokes and Euler Equations, *von Karman Institute for Fluid Dynamics Lecture Series* (1982).

[9] C. L. Merkle and M. Athavale, Time-Accurate Unsteady Incompressible Flow Algorithms Based on Artificial Compressibility, AIAA paper 87-1137, *Proceedings of AIAA 8th Computational Fluid Dynamics Conference* (1987).

[10] S. Venkateswaran, C. L. and Merkle, Analysis of Preconditioning Methods for the Euler and Navier-Stokes Equations, *von Karman Institute Lecture Series* (1999).

[11] S. Lee and D. W. Choi, On Coupling the Reynolds-averaged Navier-Stokes Equations with Two-equation Turbulence Model Equations, *International Journal for Numerical Methods in Fluids*, 50 (2) (2006) 165-197.

[12] C. Liu, X. Zheng and C. H. Sung, Preconditioned Multigrid Methods for Unsteady Incompressible Flows, *Journal of Computational Physics*, 139 (1) (1998) 35-57.

[13] A. Larsen, Advances in Aeroelastic Analysis of Suspension and Cable-Stayed Bridges, *Journal of Wind Engineering and Industrial Aerodynamics*, 74-76 (1998) 73-90.

[14] Fluent. Inc, *FLUENT 6.1 User's Guide* (2003).

Ilyong Yoo is a Ph.D. candidate in Aerodynamic Analysis and Design Laboratory at Inha University. He received his B.S. and M.S. degrees in Aerospace Engineering from Inha University in 2004 and 2006, respectively. His research area includes computational fluid dynamics, and its application to active flow control using MEMS devices.

Einkeun Kwak is a Ph.D. candidate in Aerodynamic Analysis and Design Laboratory at Inha University. He holds B.S. and M.S. degrees in Aerospace Engineering from Inha University. His research area includes computational fluid dynamics, and its application to supersonic inlet analysis and design.

Seungsoo Lee is a professor in Aerospace Engineering at Inha University. Prior to joining the faculty at Inha University, he was a senior research engineer at the Agency for Defense Development. He earned his Ph.D. degree from the Pennsylvania State University in 1990. He also holds B.S. and M.S degrees in Aeronautical and Astronautical Engineering from Seoul National University. Dr. Lee's research interests are in the area of computational fluid dynamics, overset grid method, and applied aerodynamics.

Beom Soo Kim received his B.S. and M.S degrees in Aeronautical and Astronautical Engineering from Seoul National University in 1974 and 1977, respectively. He earned his Ph.D. degree from University of Oklahoma in 1983. Dr. Kim is currently a Professor at the Department of Aerospace Engineering at Inha University. Dr. Kim's research interests are in the area of hypersonic aerodynamics, and wind tunnel testing.

Si Hyong Park is a developer in the applied analysis team of MidasIT Co. Ltd, Korea. He received the Bachelor, the Master and the Ph.D degree in Aerospace Engineering from Seoul National University in 1996, in 1998 and in 2003, respectively. His research interest is currently development of CAE software including FEM, CFD and Multi-physics simulation.